Large-eddy simulation of passive scalar with phase relaxation time in isotropic turbulence

Hiromichi Kobayashi [1,2,*] and Toshiyuki Gotoh [2,3]
[1] *Department of Physics, Hiyoshi Campus, Keio University, 4-1-1 Hiyoshi, Kohoku-ku, Yokohama 223-8521, Japan*
[2] *Research and Education Center for Natural Sciences, Hiyoshi Campus, Keio University, 4-1-1 Hiyoshi, Kohoku-ku, Yokohama 223-8521, Japan*
[3] *Department of Engineering, Nagoya Institute of Technology, Nagoya 466-8555, Japan*

(Received 7 January 2026; revised 22 May 2026; accepted 26 May 2026; published 18 June 2026)

Supersaturation in clouds was modeled as a passive scalar with the phase-relaxation time under mean uniform vertical gradient. The theoretical prediction that there exist two $-5/3$ power-law ranges in the supersaturation variance spectrum was examined using direct numerical simulation (DNS) and large-eddy simulation (LES). Although DNS at a Taylor microscale Reynolds number of 946 suggested the existence of two $-5/3$ ranges, the results were not conclusive because of the limited extent of the inertial-convective range. To achieve a wider inertial-convective range, LES was employed, and a modified eddy diffusivity model for a passive scalar without a phase-relaxation term was developed to yield a $k^{-5/3}$-spectrum across a broad range of wave numbers. LES results obtained by varying the phase-relaxation time demonstrated the coexistence of two $k^{-5/3}$ spectral ranges with different amplitudes. As the phase-relaxation time decreased, the transition between the two ranges shifted toward higher wave numbers, which is consistent with theoretical predictions. Furthermore, the probability density function (PDF) of the band-pass-filtered supersaturation indicated that the PDF tails at small scales became increasingly elongated depending on the ratio of the turbulence timescale to the phase-relaxation time.

DOI: 10.1103/zzrf-bclm

I. INTRODUCTION

Although clouds are ubiquitous, our understanding of cloud microphysical processes, such as the nucleation, growth, and evaporation of cloud droplets under the influence of turbulent mixing and convection, remains limited [1–5]. The supersaturation of water vapor and its interaction with cloud droplets are of central importance in the fundamental physics of cloud turbulence because the growth rate of cloud droplets is strongly coupled with supersaturation, and rain initiation is closely related to supersaturation fluctuations.

Numerous studies have investigated the statistical properties of the supersaturation in cloud turbulence [6–8]. A typical setup used in the study is as follows: a cubic domain of size L, significantly smaller than a cloud of size L_{cloud}, is in the core cloud region. The mean temperature T and mean supersaturation S change in the vertical direction and their mean gradients $dT/dz = \Gamma_T$ and $dS/dz = \Gamma_s$ are assumed to be constant over distance $L(\ll L_{\mathrm{cloud}})$. Within the box, the equations for the airflow velocity, temperature, supersaturation, and cloud droplets with attributes of position, velocity, temperature, and water mass are computed numerically to obtain

*Contact author: hkobayas@keio.jp

various statistics. Among the statistical quantities, the size distribution of the droplets is of central importance and is affected by supersaturation fluctuations. To simplify the theoretical analysis, it is assumed that the supersaturation is simply mixed by turbulent airflow and does not react to the velocity and temperature. Accordingly, supersaturation is treated as a passive scalar that is transferred by an incompressible airflow and changes its amplitude due to the evaporation (or condensation) of cloud droplets at a rate of $1/\tau_s$. Then, the governing equation for supersaturation fluctuation s is given by

$$\frac{\partial s}{\partial t} + \boldsymbol{u} \cdot \nabla s = -\frac{1}{\tau_s} s + \kappa \nabla^2 s + \Gamma_s u_3, \tag{1}$$

where $\boldsymbol{u}$ and u_3 represent the velocity and its component in the vertical direction, respectively, and κ is the supersaturation diffusion coefficient. Because $L \ll L_{\text{cloud}}$, τ_s is treated as a constant that depends on the mean temperature and pressure inside the box. A detailed derivation of the phase-relaxation time and Eq. (1) is presented in Appendix A [7].

The phase-relaxation time τ_s is scale-independent, whereas the characteristic time of turbulent motion $\tau_f(r)$ decreases with the scale r of fluid motion. Consequently, there exists a crossover scale r_s defined by $\tau_s = \tau_f(r_s)$. From a dynamic perspective, these different characteristic timescales in a system lead to different behaviors of the system. At a scale $r > r_s$, τ_s is shorter than the turbulent mixing time $\tau_f(r)$; hence, the phase change proceeds more rapidly than the turbulent mixing. In this regime, supersaturation in an air blob of size r can quickly adjust to the ambient air, leading to a homogeneous distribution of the supersaturation. Conversely, the supersaturation within an eddy of scale $r < r_s$ remains largely unchanged during the mixing process, resulting in a spatially inhomogeneous and rapidly varying distribution. These arguments suggest that the statistical properties of supersaturation differ significantly depending on scale.

Several studies have been conducted on the probability density function (PDF) of supersaturation fluctuations and their variance as a measure of the PDF broadness in terms of the Langevin model for supersaturation, with phenomenological arguments and parameters [8,9]. However, studies on the spectrum of supersaturation (or water vapor) from the viewpoints of fundamental physics are limited, despite their importance in cloud microphysics. This is partly due to the difficulty of directly measuring supersaturation compared with liquid water content (LWC). Establishing the statistical theory of supersaturation fluctuations and comparing it with measured data are essential for deepening our understanding of the cloud turbulence and for developing improved models for cloud microphysics simulations.

As a phenomenological argument, Mazin [10] argues that the spectrum of cloud LWC has two $k^{-5/3}$ spectral ranges. Gotoh *et al.* [7] have shown the following using the spectral theory of turbulence:

$$E_s(k) = \begin{cases} \frac{2}{3}(\tau_s\Gamma_s)^2 E(k) = \frac{2}{3}(\tau_s\Gamma_s)^2 K \varepsilon^{2/3} k^{-5/3} & \text{for} \quad k \ll k_s, \\ C_{\text{OC}} \chi \varepsilon^{-1/3} k^{-5/3} & \text{for} \quad k_s \ll k, \end{cases} \tag{2}$$

where $k = 2\pi/r$, ε and χ denote the mean rates of energy dissipation and variance destruction, respectively, and K and C_{OC} are the Kolmogorov and Obukhov-Corrsin constants, respectively [11–13]. The derivation of Eq. (2) is detailed in Appendix B. Although each spectrum follows a $k^{-5/3}$ power law with a different amplitude, the underlying physics behind the two ranges differs: The low-wave-number range is driven by direct excitation from the vertical velocity u_3, whereas the high-wave-number range is governed by the cascade of the scalar variance through the wave-number space.

Accordingly, it is necessary to verify the theoretical prediction of the supersaturation spectrum. One approach is to use a large-scale numerical simulation. The inertial range of the kinetic energy spectrum must be sufficiently wide for the two $k^{-5/3}$ spectra to coexist. However, an approach using direct numerical simulation (DNS) on a state-of-the-art high-performance computer faces significant challenges because a considerable portion of the wave-number space is devoted to simulating small-scale dynamics within the dissipation range.

An alternative method is to conduct a large-eddy simulation (LES); however, there is another problem. To obtain the two $k^{-5/3}$ spectra for supersaturation, the $k^{-5/3}$ range of the kinetic energy spectrum must be wider than the total widths of the two $k^{-5/3}$ ranges for supersaturation. A simple estimate suggests that the supersaturation spectrum in Eq. (2) requires one decade for the $k^{-5/3}$ range at $k < k_s$, another decade for the $k^{-5/3}$ range at $k > k_s$, and one decade for the transition between them, yielding a total of approximately three decades. This implies an LES with grid resolution comparable to that of a massive DNS. To our knowledge, no LES with such a large number of grid points has been conducted to obtain the wider inertial range. Furthermore, it remains uncertain whether the conventional subgrid-scale (SGS) models of the LES for both the velocity and scalar can accurately establish a wide inertial-convective range.

The purpose of this study is twofold. First, we develop an LES scheme for velocity and supersaturation that incorporates the inherent characteristic time allowing an inertial-convective range spanning three orders of magnitude in the wave number. One concern is the use of the SGS model for passive scalar. Previous studies have indicated that the spectral eddy diffusivity is not constant with respect to wave number but increases as wave number decreases, suggesting that a wide $k^{-5/3}$ spectrum is not available in an LES with conventional spectral eddy diffusivity. Therefore, we modify the SGS model. Next, we examine the supersaturation variance spectrum by changing the phase-relaxation time τ_s using the newly developed eddy diffusivity. Additionally, we analyze the PDF of the filtered supersaturation to investigate how the PDF shape evolves across the spatial scale and to assess the effects of small-scale intermittency.

The remainder of this paper is organized as follows: In Sec. II, the fundamental equations for velocity and supersaturation are established. The DNS results are presented in Sec. III. In Sec. IV, the LES equations with spectral eddy viscosity and modified eddy diffusivity are described for a passive scalar without a phase-relaxation term. In Sec. V, supersaturation spectra with finite relaxation times are examined in an LES by varying the phase-relaxation time. In Sec. VI, the intermittency of the supersaturation in the two ranges is studied by examining the PDF of the filtered supersaturation. Finally, Sec. VII summarizes our findings.

II. EQUATIONS AND STATISTICAL QUANTITIES

We consider supersaturation fluctuation s using the same setup described in the previous section [7]. The fluid velocity $\boldsymbol{u}$ is assumed to obey the continuity and Navier-Stokes equations, and the advection-diffusion equation for supersaturation is rewritten for subsequent analysis:

$$\nabla \cdot \boldsymbol{u} = \boldsymbol{0}, \tag{3}$$

$$\frac{\partial \boldsymbol{u}}{\partial t} + \boldsymbol{u} \cdot \nabla \boldsymbol{u} = -\nabla P + \nu \nabla^2 \boldsymbol{u} + \boldsymbol{f}, \tag{4}$$

$$\frac{\partial s}{\partial t} + \boldsymbol{u} \cdot \nabla s = -\frac{1}{\tau_s} s + \kappa \nabla^2 s + \Gamma_s u_3, \tag{5}$$

where P, ν, and $\boldsymbol{f}$ denote pressure, kinetic viscosity, and external forces, respectively.

The DNS of the above set of equations is conducted in a cubic box of length $L = 2\pi$. The pseudospectral method is used for spatial discretization, and the Runge-Kutta-Gill method is used for time advancement [14]. The external force $\boldsymbol{f}$ is assumed to obey the Ornstein-Uhlenbeck process with Gaussian statistics. Its statistical properties in wave-number space are specified as

$$\langle \boldsymbol{f}(\boldsymbol{k}, t) \rangle = 0, \tag{6}$$

$$\langle \boldsymbol{f}(\boldsymbol{k}, t) \cdot \boldsymbol{f}(-\boldsymbol{k}, s) \rangle = \begin{cases} \frac{D_0}{4\pi k^2} e^{-\sigma_0 (t-s)} & \text{for} \quad k_1 \leqslant k \leqslant k_2, \\ 0 & \text{otherwise,} \end{cases} \tag{7}$$

where $\langle\,\rangle$ represents the ensemble average and $k^2 = k_j k_j$. D_0 denotes the variance of the external force and is related to the kinetic energy dissipation rate per unit mass as $\varepsilon = \sigma_0^{-1} D_0 \Delta k$ in a statistically steady state. Here, $\Delta k = k_2 - k_1$, and the parameters are chosen to be $D_0 = 0.3$, $\sigma_0 = 1$, $[k_1, k_2] = [1.4]$ for D1 and all LESs, and $[1, 2]$ for D2 in the present study. The Schmidt number $\mathrm{Sc} = \nu/\kappa\ 0.72$ is adopted, and $\Gamma_s = 1$ without loss of generality due to the linearity of the equation for s. The double and triple aliasing errors are removed by truncating the wave-vector components for $k > (2\sqrt{2}/3)(N/2) = k_c$, where k_c denotes the cutoff wave number.

For the velocity field, the kinetic energy spectrum $E(k)$ is defined as

$$E = \frac{1}{2}\langle u^2\rangle = \frac{3}{2}\overline{u}^2 = \int_0^\infty E(k)dk, \tag{8}$$

where $\overline{u}$ denotes the root-mean-square velocity [15]. Then, the mean energy dissipation rate ε, integral scale L_u, Taylor microscale λ, Kolmogorov scale length η, and Reynolds number R_λ are defined as

$$\varepsilon = 2\nu \int_0^\infty k^2 E(k)dk, \qquad L_u = \left(\frac{3\pi}{4}\int_0^\infty k^{-1}E(k)dk\right)E^{-1},$$
$$\lambda = \left(\frac{5E}{\int_0^\infty k^2 E(k)dk}\right)^{1/2}, \quad \eta = \left(\frac{\nu^3}{\varepsilon}\right)^{1/4}, \quad R_\lambda = \frac{\overline{u}\lambda}{\nu}, \tag{9}$$

respectively. For supersaturation, the variance spectrum $E_s(k)$ is defined as follows:

$$E_s = \langle s^2\rangle = \overline{s}^2 = \int_0^\infty E_s(k)dk, \tag{10}$$

where $\overline{s}$ denotes the root-mean-square supersaturation [16]. The mean destruction rate of variance χ, the integral scale L_s, and the Batchelor length η_s are defined as

$$\chi = 2\kappa \int_0^\infty k^2 E_s(k)dk, \quad L_s = \left(\frac{\pi}{2}\int_0^\infty k^{-1}E_s(k)dk\right)E_s^{-1}, \quad \eta_s = \frac{1}{\mathrm{Sc}}\eta, \tag{11}$$

respectively.

Note that, strictly speaking, the statistics of supersaturation are axis-symmetric due to the vertical forcing. Consequently, the spectrum $\langle s(\boldsymbol{k})s(-\boldsymbol{k})\rangle$ (where $\boldsymbol{k}$ is the wave-number vector) can be expanded in terms of the Legendre polynomials. In this study, we focus on the isotropic part (the zeroth-order term) of this expansion, as it provides the dominant contribution to the overall energy. All spectra reported are calculated as spherical-shell averages to extract this isotropic component. Further details can be found in Eqs. (16)–(23) of Ref. [17].

III. DNS RESULTS

We performed Runs D1 and D2 for supersaturation with $\tau_s = \infty$ in homogeneous isotropic turbulence. Run D1 was conducted to study the spectral eddy viscosity and diffusivity; the results are discussed in Sec. IV. Run D2 was performed to investigate the behavior of supersaturation spectrum resolved by DNS at $R_\lambda = 946$ with $N = 4096^3$ grid points. After the transient period, the numerical solutions for $\tau_s = \infty$ entered a statistically steady state.

Turbulence statistics were gathered from a given time t_0 as the time average over 11.7 T_e for D1 and 3.34 T_e for D2 in the statistically steady state, where $T_e = L_u/\overline{u}$ denotes the large-eddy turnover time. Statistical velocity and supersaturation data for $\tau_s = \infty$ and the numerical parameters are presented in Table I. The spatial resolution criterion is known as $k_c\eta \geqslant 1.5$, for which the smallest dissipation field is adequately resolved. The present numerical data for Runs D1 and D2 indicate $k_c\eta = 1.4$ and 1.5, respectively, which is satisfactory for the present study, as our objective is to examine the existence of two $k^{-5/3}$ spectra. For finite relaxation times, Runs D2-1, D2-2, and

TABLE I. Turbulence statistics and numerical parameters for DNS and LES for $\tau_s = \infty$.

	Run	N	k_c	R_λ	ν $(\times 10^{-5})$	E	E_s	L_u	L_s	ε, ε_T	χ, χ_T	η $(\times 10^{-3})$	η_s $(\times 10^{-3})$
DNS	D1	1024^3	483	273	25.0	0.814	1.15	0.439	0.697	0.240	0.749	2.84	3.94
DNS	D2	4096^3	1932	946	5.0	1.58	1.92	1.27	0.796	0.361	1.18	0.767	1.07
LES	L1	128^3	60		0.025	1.21	3.13	0.671	0.874	0.241	1.80		
LES	L2	512^3	240		0.025	3.96	4.75	0.566	0.764	1.78	5.69		
LES	L3	1024^3	483		0.025	1.90	2.65	0.538	0.804	0.624	2.04		

D2-5 (corresponding to $\tau_s = 0.1, 0.2, 0.5$, respectively), started from *initial* conditions of the same velocity and supersaturation at t_0 but with independent random forces. After the transient period, the three runs reached statistically steady states. All spectra $E_s(k)$ were computed as the time averages over durations of 1.9, 4.2, 2.1, and 2.0 in units of T_e. The normalized phase-relaxation times τ_s/T_e are presented in Table II.

Figure 1 shows the compensated spectra of the kinetic energy $\varepsilon^{-2/3}k^{5/3}E(k)$ and supersaturation variance $\chi^{-1}\varepsilon^{1/3}k^{5/3}E_s(k)$ for $\tau_s = 0.1, 0.2, 0.5$, and ∞ from Run D2 at $R_\lambda = 946$. The horizontal lines represent the Kolmogorov constant $K = 1.6$ and Obukhov-Corrsin constant $C_{\mathrm{OC}} = 0.69$, respectively. When τ_s is infinite, the compensated curve for $E_s(k)$ settles at C_{OC} at low wave numbers. As τ_s decreases, the curve gradually departs from $C_{\mathrm{OC}} = 0.69$, shifting toward $K = 1.6$ at low wave numbers, and the width of the horizontal curve at low wave numbers widens near $K = 1.6$. This trend becomes increasingly apparent with a reduction in τ_s. The characteristic turbulence time $\tau_f(k)$ in the inertial range is given by

$$\tau_f(k) = \left(\int_0^k p^2 E(p)dp\right)^{-1/2} = \sqrt{\frac{4}{3}}\, K^{-1/2}\varepsilon^{-1/3}k^{-2/3}. \tag{12}$$

Using the turbulence data in Table I, we can estimate the wave number k_s as $k_s\eta \approx (0.31, 1.2, 3.5) \times 10^{-2}$ for $\tau_s = (0.5, 0.2, 0.1)$, respectively. Although these $k_s\eta$ values are smaller than those seen in Fig. 1, the trend of increasing $k_s\eta$ with decreasing τ_s is consistent with the observations in Fig. 1.

However, the DNS results are not conclusive. The wave-number width of the transition of the curve from $C_{\mathrm{OC}} = 0.69$ to $K = 1.6$ is approximately one decade, and no part of the compensated spectrum for $E_s(k)$ settles at C_{OC} at high wave numbers. This is because the right tail of the $k^{-5/3}$ spectrum of $E_s(k)$ is masked by a bump and rapid decay of the spectrum under diffusive effects. Therefore, more definite conclusions regarding the coexistence of the two $k^{-5/3}$ spectra require a sufficiently wide inertial-convective range for scalars spanning the entire wave-number space in the simulations, suggesting the use of LES.

TABLE II. Phase-relaxation time normalized by the large-eddy turnover time.

DNS				LES											
Run	T_e	τ_s	τ_s/T_e	Run	T_e	τ_s	τ_s/T_e	Run	T_e	τ_s	τ_s/T_e	Run	T_e	τ_s	τ_s/T_e
D1	0.596	∞	∞	L1	0.747	∞	∞	L2	0.348	∞	∞	L3	0.478	∞	∞
D2	1.24	∞	∞	L1-05	0.747	0.05	0.067	L2-05	0.348	0.05	0.144	L3-005	0.478	0.005	0.011
D2-1	1.24	0.1	0.081	L1-1	0.747	0.1	0.134	L2-1	0.348	0.1	0.287	L3-01	0.478	0.01	0.021
D2-2	1.24	0.2	0.161	L1-2	0.747	0.2	0.268	L2-2	0.348	0.2	0.575	L3-1	0.478	0.1	0.209
D2-5	1.24	0.5	0.403	L1-5	0.747	0.5	0.669	L2-5	0.348	0.5	1.44	L3-2	0.478	0.2	0.418
												L3-5	0.478	0.5	1.05

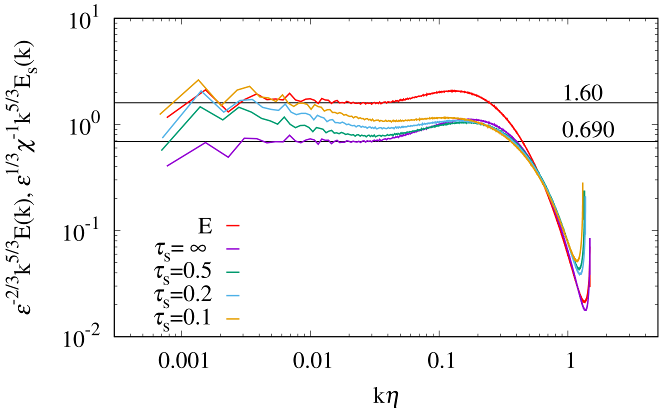

FIG. 1. Compensated spectra $\chi^{-1}\varepsilon^{1/3}k^{5/3}E_s(k)$ and $\varepsilon^{-2/3}k^{5/3}E(k)$ (red) at $R_\lambda = 946$ by DNS with $N = 4096^3$. Magenta: $\tau_s = \infty$, green: $(\tau_s, k_s\eta) = (0.5, 0.0031)$, cyan: $(0.2, 0.012)$, orange: $(0.1, 0.35)$. Horizontal lines indicate the Kolmogorov constant $K = 1.60$ and Obukhov-Corrsin constant 0.69, respectively.

IV. LES OF SUPERSATURATION

The LES equations in the wave-vector space are as follows:

$$u_i^<(\boldsymbol{k}) = F(k|k_c)u_i(\boldsymbol{k}), \qquad s^<(\boldsymbol{k}) = F(k|k_c)s(\boldsymbol{k}), \tag{13}$$

$$\left(\frac{d}{dt} + \nu_T(k|k_c)k^2\right)u_i^<(\boldsymbol{k}, t) = F(k|k_c)M_{ijl}(\boldsymbol{k})\sum^{\Delta} u_j^<(\boldsymbol{p}, t)u_l^<(\boldsymbol{q}, t) + f_i(\boldsymbol{k}, t), \tag{14}$$

$$\left(\frac{d}{dt} + \kappa_T(k|k_c)k^2 + \frac{1}{\tau_s}\right)s^<(\boldsymbol{k}, t) = F(k|k_c)C_i(\boldsymbol{k})\sum^{\Delta} u_i^<(\boldsymbol{p}, t)s^<(\boldsymbol{q}, t) + \Gamma u_3^<(\boldsymbol{k}, t), \tag{15}$$

$$M_{ijl}(\boldsymbol{k}) = -i\frac{1}{2}[k_l P_{ij}(\boldsymbol{k}) + k_j P_{il}(\boldsymbol{k})], \quad P_{ij}(\boldsymbol{k}) = \delta_{ij} - \frac{k_i k_j}{k^2}, \tag{16}$$

$$C_i(\boldsymbol{k}) = -ik_i, \tag{17}$$

where $\nu_T(k|k_c)$ and $\kappa_T(k|k_c)$ denote the wave-number-dependent eddy viscosity and diffusivity, respectively, and $\sum^{\Delta}$ denotes the sum of the triad terms satisfying $\boldsymbol{k} = \boldsymbol{p} + \boldsymbol{q}$. $F(k|k_c)$ represents the sharp cutoff filter at k_c:

$$F(k|k_c) = \begin{cases} 1 & \text{for } k \leqslant k_c \\ 0 & \text{for } k > k_c \end{cases}. \tag{18}$$

The spectra in the LES are defined as

$$E^<(k) = 2\pi k^2\langle u_i^<(\boldsymbol{k})u_i^<(-\boldsymbol{k})\rangle, \quad E_s^<(k) = 4\pi k^2\langle s^<(\boldsymbol{k})s^<(-\boldsymbol{k})\rangle. \tag{19}$$

The $\nu_T(k|k_c)$ and $\kappa_T(k|k_c)$ are defined in terms of the transfer functions contributing to modes $\boldsymbol{u}^<(\boldsymbol{k})$ and $s^<(\boldsymbol{k})$ with $k < k_c$ from excitations satisfying p or $q > k_c$ for triad interactions as

$$\nu_T(k|k_c) = -\frac{T^>(k)}{2k^2E^<(k)}, \tag{20}$$

$$\kappa_T(k|k_c) = -\frac{T_\theta^>(k)}{2k^2E_\theta^<(k)}, \tag{21}$$

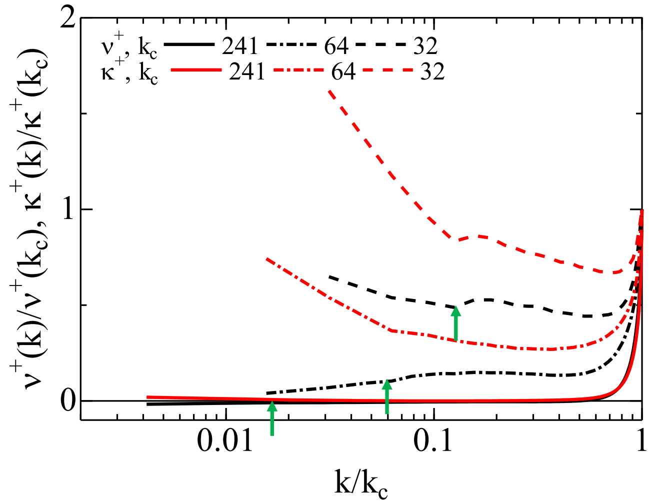

FIG. 2. Normalized spectral eddy viscosity and diffusivity for cutoff wave numbers $k_c = 32$, 64, and 241 in $\tau_s = \infty$, obtained *a priori* from DNS Run D1 using Eqs. (20) and (21). Green arrows on the eddy viscosity spectra indicate the forcing wave number $k_2 = 4$ ($[k_1, k_2] = [1, 4]$).

where

$$T^>(k) = -\sum_{k\ \mathrm{shell}}\left[M_{ijl}(\boldsymbol{k})\sum^{\Delta} u_j(\boldsymbol{p})u_l(\boldsymbol{q}) - F(k|k_c)M_{ijl}(\boldsymbol{k})\sum^{\Delta} u_j^<(\boldsymbol{p})u_l^<(\boldsymbol{q})\right], \tag{22}$$

$$T_s^>(k) = -\sum_{k\ \mathrm{shell}}\left[C_i(\boldsymbol{k})\sum^{\Delta} u_i(\boldsymbol{p})s(\boldsymbol{q}) - F(k|k_c)C_i(\boldsymbol{k})\sum^{\Delta} u_i^<(\boldsymbol{p})s^<(\boldsymbol{q})\right], \tag{23}$$

respectively [18]. Then the dissipation and destruction rates due to the eddy viscosity and diffusivity are computed as

$$\varepsilon_T = 2\int_0^{k_c} \nu_T(k|k_c)k^2E^<(k)dk, \tag{24}$$

$$\chi_T = 2\int_0^{k_c} \kappa_T(k|k_c)k^2E_s^<(k)dk, \tag{25}$$

respectively. The numerical method for LES is identical to that for DNS, and a very low molecular viscosity and diffusivity are included for numerical stability. The molecular viscosity for LES is set to $\nu = 2.5 \times 10^{-7}$ as listed in Table I. The corresponding molecular diffusivity (supersaturation diffusion coefficient) is set to $\kappa = \nu/\mathrm{Sc}$. The numerical parameters are presented in Tables I and II.

Before LES is applied to the problem, when $1/\tau_s$ terms are absent (infinite τ_s), it is necessary to examine whether the eddy viscosity and diffusivity of the model establish $k^{-5/3}$ power-law spectra for both $E(k)$ and $E_s(k)$ over the entire wave-number range used in the LES with a large number of grid points. The reason for the examination is that the wave-number dependence of $\nu_T(k|k_c)$ and $\kappa_T(k|k_c)$ for $k \ll k_c$ by the simulation differs from the prediction of the spectral theory [18,19]. The spectral theory tells that for $E(k)$ and $E_s(k)$ to be $k^{-5/3}$, both $\nu_T(k|k_c)$ and $\kappa_T(k|k_c)$ must be independent of k for $k \ll k_c$ [18,19]. As for the numerical examination, we used DNS data for an *apriori* test of the models because, when LES data are used, unexpected side effects related to the eddy viscosity and diffusivity may enter the results.

Figure 2 shows the spectral eddy viscosity (black) and diffusivity (red) computed *a priori* from DNS data (Run D1) using Eqs. (20) and (21) for $k_c = 32$, 64, and 241. Common feature of the

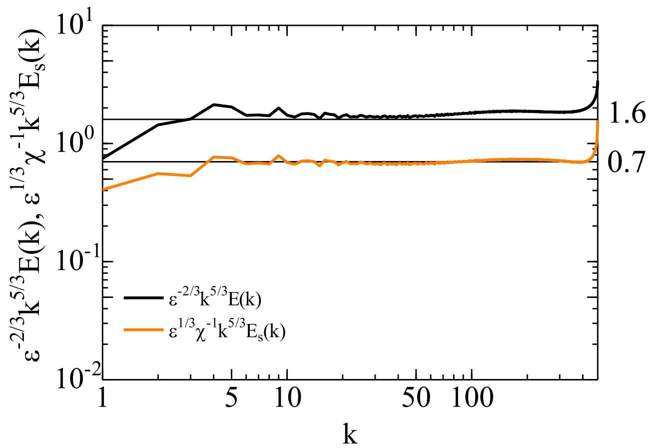

FIG. 3. Compensated spectra from LES Run L3. Black: $\varepsilon_T^{-2/3}k^{5/3}E(k)$, orange: $\chi_T^{-1}\varepsilon_T^{1/3}k^{5/3}E_s(k)$ with $\tau_s = \infty$. Horizontal lines indicate $K = 1.6$ and $C_{\rm OC} = 0.7$, respectively.

curves is that they have cusps near $k/k_c = 1$, and the values increase with decrease of k_c. The latter is due to the fact that their amplitudes are in proportion to the amount of kinetic energy residing in the range $k > k_c$ [18]. For $k_c = 241$, the total amount of kinetic energy in the (dissipation) range $k > k_c$ (since the DNS can resolve the dissipation range) is so small that the two curves at low wave numbers appear to be collapsing. In the low-wave-number range of $k/k_c \ll 1$, they behave differently. $\nu_T(k|k_c)$ is roughly constant, while $\kappa_T(k|k_c)$ increases as k becomes small and the increase rate grows with the decrease of k_c; for example, $\kappa_T(k|k_c)$ for $k_c = 32$ increases from about 0.75 to 1.6 as k/k_c moves from 0.7 toward 0.03.

Since the constancy of the eddy diffusivity at $k < k_c$ is essential for sustaining the $k^{-5/3}$-spectrum inertial range in LES [18], this wave-number dependence of the eddy diffusivity suggests a deviation of the scalar spectrum in LES from the $k^{5/3}$ power law. Therefore, when $\kappa_T(k|k_c)$ predicted by spectral theory is straightforwardly applied to the present LES [19,20], it is uncertain whether the $k^{-5/3}$ power-law spectra of the scalar variance are established over the entire wave-number band used in the simulation. Indeed, we find in Appendix C that $E_s(k)$ (without the phase relaxation term) computed by LES with the conventional spectral eddy diffusivity type 1 [Eq. (C4)] deviates from the $k^{-5/3}$ power law, as shown in Fig. 7. The reason for this slow increase is unknown and should be explored in future studies. In the present study, we proceed to modify the spectral eddy diffusivity by trial and error so as to yield the $k^{-5/3}$ power law over the entire wave numbers, which is described in Appendix C.

A modified eddy diffusivity in the present study is given by

$$\nu_T(k|k_c) = f(k/k_c)\sqrt{E(k_c)/k_c}, \quad f(x) = C_m[0.441 + 15.2\exp(-3.03/x)], \tag{26}$$

$$\kappa_T^{(3)}(k|k_c) = 1.3\frac{1}{\mathrm{Sc}_T}g(k/k_c)\sqrt{E(k_c)/k_c}, \quad g(x) = C_m\exp(-2.4x) + f(x), \tag{27}$$

where $C_m = 0.3$ for Runs (L1, L2), 0.6 for Run L3, and $\mathrm{Sc}_T = 0.72$. The factor $\sqrt{E(k_c)/k_c}$ is introduced to account for the velocity excitation at the cutoff wave number k_c. The first term of $g(x)$ in Eq. (27) is introduced to take into account the increase in the eddy diffusivity as the wave number decreases, as shown in Fig. 2.

Figure 3 presents the compensated spectra of $\varepsilon^{-2/3}k^{5/3}E(k)$ and $\chi^{-1}\varepsilon^{1/3}k^{5/3}E_s(k)$ obtained from LES Run L3 using Eqs. (26) and (27). The two curves are almost horizontal at $K = 1.6$ and $C_{\rm OC} = 0.7$, respectively. In the following, we study the spectrum of the supersaturation variance for various τ_s values using LES with the modified eddy diffusivity.

V. SPECTRA OF SUPERSATURATION VARIANCE WITH FINITE PHASE-RELAXATION TIME

We now consider the influence of τ_s on the scalar variance spectrum $E_s(k)$. Hereafter, the superscripts $^<$ in $E^<(k)$ and $E_s^<(k)$ are omitted for clarity. The theoretical spectra in Eq. (2) suggest the following normalization for $E_s(k)$ by LES:

$$W^v(k) = (\Gamma_s\tau_s)^{-2}\varepsilon_T^{-2/3}k^{5/3}E_s(k), \quad \text{for} \quad k < k_s, \tag{28}$$

$$W^c(k) = \chi_T^{-1}\varepsilon_T^{1/3}k^{5/3}E_s(k), \quad \text{for} \quad k_s < k. \tag{29}$$

Notably, ε_T and χ_T are used instead of ε and χ. Therefore, when $E_s(k)$ follows Eq. (2), the spectra $W^v(k)$ and $W^c(k)$ for a finite τ_s approach the constants as

$$W^v(k) = \tfrac{2}{3}K \approx 1.07, \quad \text{for} \quad k \ll k_s, \tag{30}$$

$$W^c(k) = C_{\mathrm{OC}} \approx 0.7, \quad \text{for} \quad k_s \ll k, \tag{31}$$

where $K = 1.6$ is used.

Figure 4 shows the spectra $W^v(k)$ and $W^c(k)$ for different τ_s values when the number of grid points is (a) $N = 128^3$, (b) 512^3, and (c) 1024^3. In Fig. 4(a), the curve of $W^c(k)$ for $\tau_s = \infty$ (orange) is close to the horizontal line at $C_{\mathrm{OC}} = 0.7$. In contrast, the black curve of $W^v(k)$ for $\tau_s = 0.01$ is approximately a horizontal line at 1.25 (>1.07) for $k \geqslant 4$. The turbulence characteristic time $\tau_f(k)$ (magenta) is also plotted, and $\tau_f(k_c)$ at the cutoff wave number k_c is slightly smaller than 0.1. For example, for $\tau_s = 0.1$, $\tau_f(k)$ crosses the horizontal line at 0.1 at $k_s \approx 50$, and $W^c(k_s)$ (green) is approximately 0.9 (>0.7). This suggests that deviation from the orange curve occurs at wave numbers considerably larger than k_c. For $\tau_s = 0.2$, we have $k_s \approx 23$, at which the blue curve begins to depart from the orange curve as the wave number decreases. However, it is uncertain whether the left tail of $W^c(k)$ tends toward a constant,

$$k^{5/3}\chi_T^{-1}\varepsilon_T^{1/3}E_s(k) = \frac{2}{3}K(\Gamma_s\tau_s)^2\frac{\varepsilon_T}{\chi_T} \equiv J^c(\tau_s), \tag{32}$$

which follows from substitution of Eq. (2). Therefore, we conclude that LES Run L1 is not sufficient for observing the coexistence of two $k^{-5/3}$ power-law spectra in $E_s(k)$. In Fig. 4(b), the curve $(2/3)\varepsilon^{-2/3}k^{5/3}E(k)$ is also plotted in red and is close to the curve $W^v(k)$ (black) for $\tau_s = 0.01$. The curves $W^c(k)$ for $\tau_s > 0.05$ exhibit a region that overlaps the orange horizontal line at approximately 0.7 at high wave numbers; as the wave number decreases, they move upward from this level, and the extent of the deviation increases with decreasing τ_s. In Fig. 4(c), the transition from $W^c(k)$ to $W^v(k)$ occurs in the wave-number range of $10 < k < 100$. At $\tau_s = 0.5$, the deviation point from the orange curve is approximately 32, and it shifts to higher wave numbers with decreasing τ_s. In contrast, the low-wave-number part of the curve approaches J^c, and for $\tau_s \leqslant 0.01$, the curves $W^v(k)$ (black) are approximately horizontal at 1.07. These observations are consistent with the theoretical prediction that in the supersaturation variance spectrum, two $k^{-5/3}$ power-law ranges can coexist when the kinetic energy spectrum exhibits a sufficiently wide inertial range.

Figure 5 shows (a) unnormalized $\Pi_s(k)$ and (b) normalized $\Pi_s^*(k) = \Pi_s(k)/\chi_T$ transfer fluxes of scalar variance for LES Run L3, which are defined as

$$\Pi_s(k) = -\int_{k_{L_s}}^{k} T_s(p)\,dp, \tag{33}$$

where $k_{L_s} = 2\pi/L_s$ and $T_s(k)$ denotes the filtered transfer function of the variance due to the convective term in Eq. (5) [or (15)]. The curves in Fig. 5(a) are from the bottom for $\tau_s = 0.005$, 0.01, 0.05, 0.1, 0.2, 0.5, and ∞, respectively. $\Pi_s(k)$ is approximately constant as a function of the wave number for $5 < k < 200$ but the plateau level decreases monotonically as τ_s decreases from ∞ to 0.005. The curves for $\Pi_s^*(k)$ in Fig. 5(b) are approximately unity for $5 < k < 200$ for $\tau_s > 0.05$ despite the large variation in the plateau level as seen in Fig. 5(a). Meanwhile, the approximate

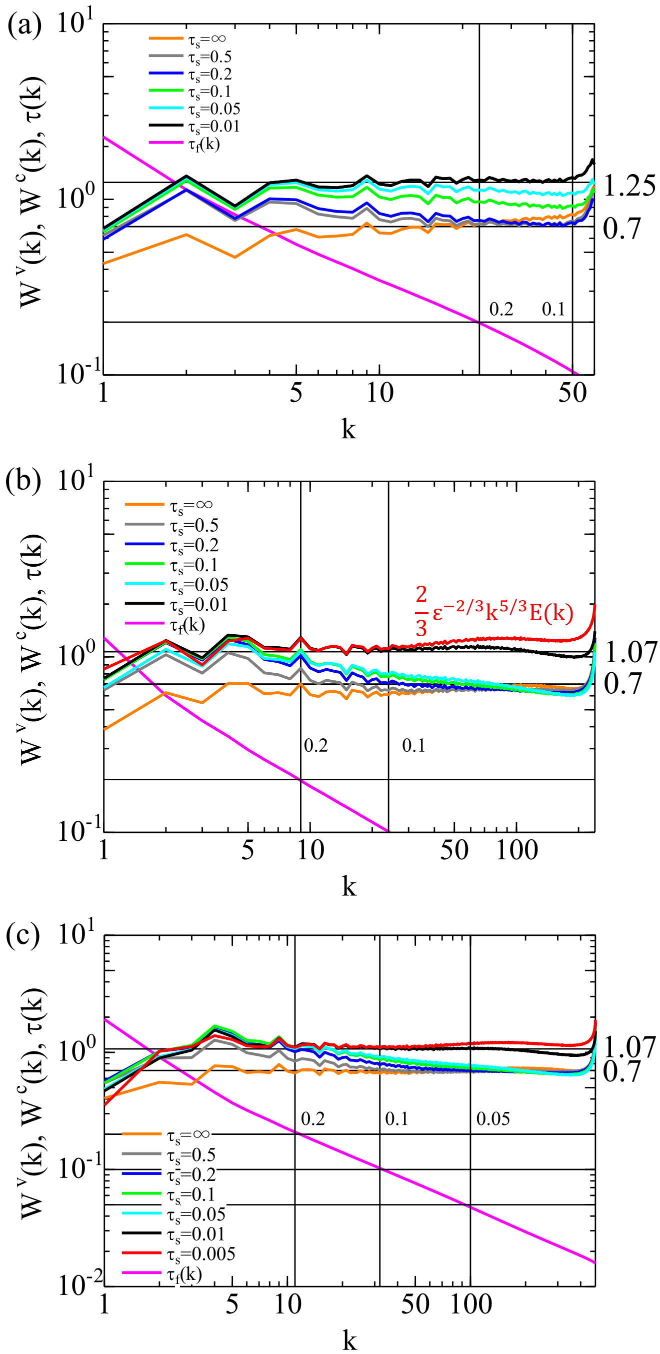

FIG. 4. Compensated scalar variance spectra for $\tau_s = 0.01, 0.05, 0.1, 0.2, 0.5$, and ∞ in (a) 128^3 ($C_m = 0.3$), (b) 512^3 ($C_m = 0.3$), and (c) 1024^3 ($C_m = 0.6$) grid points in LES. The turbulence time $\tau_f(k)$ is plotted in magenta. (a) $W^v(k)$ for $\tau_s = 0.01, 0.05, 0.1$ and $W^c(k)$ for $\tau_s = 0.2, 0.5, \infty$; (b) $W^v(k)$ for $\tau_s = 0.01$ and $W^c(k)$ for $\tau_s = 0.05, 0.1, 0.2, 0.5, \infty$, red: $(2/3)\varepsilon^{-2/3}k^{5/3}E(k)$; (c) $W^v(k)$ for $\tau_s = 0.005, 0.01$ and $W^c(k)$ for $\tau_s = 0.05, 0.1, 0.2, 0.5, \infty$. The upper horizontal lines indicate plateau values of 1.25, 1.07, and 0.7, and the lower horizontal lines correspond to $\tau_s = 0.2$ for (a) and (b), and $\tau_s = 0.2, 0.1, 0.05$ for (c). Vertical lines denote k_s satisfying $\tau_s = \tau(k_s)$.

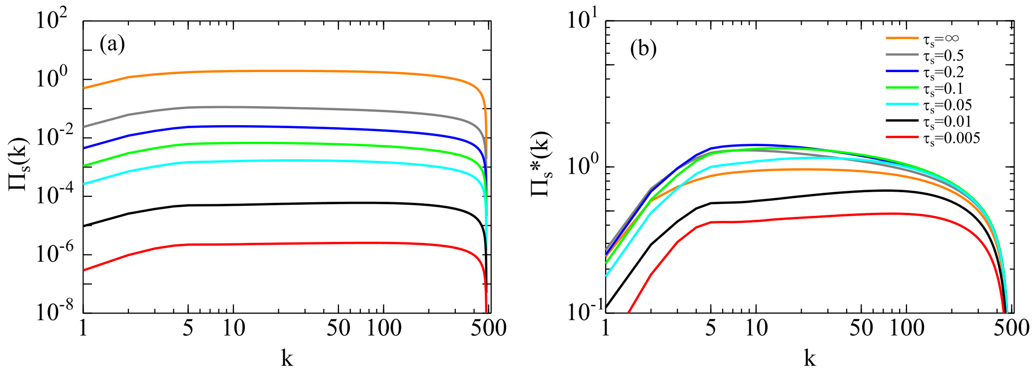

FIG. 5. Transfer fluxes for scalar variance for LES Run L3: (a) unnormalized curves are from the bottom for $\tau_s = 0, 005, 0.01, 0.05, 0.1, 0.2, 0.5, \infty$; (b) normalized by the destruction rate.

plateau levels of the curves for $\tau_s = 0.005$ and 0.01 are approximately 0.4 and 0.5, respectively, which are obtained by normalizing small Π_s by small dissipation and considerably less than unity.

The above observations provide an interpretation as to how the supersaturation fluctuations are excited. In the steady state, the spectral variance budget for Eq. (5) is written as (see Appendix B and [7])

$$\frac{\partial \Pi_s(k)}{\partial k} + \frac{2}{\tau_s} E_s(k) = \frac{4}{3}\Gamma_s^2 \tau(k) E(k), \quad \frac{1}{\tau(k)} = \frac{2}{\tau_f(k)} + \frac{1}{\tau_s}. \tag{34}$$

When τ_s is large, $\tau(k) \approx \tau_f(k)/2$ and the input $(2/3)\Gamma_s^2 \tau_f(k) E(k)$ primarily balances with $\partial \Pi_s(k)/\partial k$, meaning that the input from the kinetic energy under the uniform gradient is transferred to high wave numbers by the cascade process, establishing the Obukhov-Corrsin $k^{-5/3}$ regime. On the other hand, as τ_s is small, $\tau(k) \approx \tau_s$ and the input $(4/3)\Gamma_s^2 \tau_s E(k)$ balances with the $2E_s(k)/\tau_s$ term, meaning that most of the input from the kinetic energy goes directly to the excitation of $E_s(k)$, generating another $k^{-5/3}$ power-law range. Only a small amount of the input, giving small $\Pi_s(k)$ but being nearly constant in k, is transferred to high wave numbers, as seen in Fig. 5. Since Eq. (5) is linear, $E_s(k, t)$ is given by the sum of two contributions from two processes, both of which generate a $k^{-5/3}$ power law but with different amplitudes. The dynamics in two processes differ, and Π_s indicates the extent that the cascade process contributes to the excitation of s.

VI. PDFs FOR SUPERSATURATION

Supersaturation fluctuations at small scales strongly affect the size distributions during the initial phase of droplet growth. Figure 6 shows the total, low-pass ($k < 9$), middle-pass ($9 < k < 24$), and high-pass-filtered ($k > 24$) velocity and scalar PDFs for $\tau_s = 0.01$, 0.2, and ∞ obtained from LES Run L3. The thin black line represents the Gaussian distribution. The PDFs of the fluctuations without a filter are shown in Fig. 6(a). The PDF of u_3 is similar to the typical Gaussian distribution, and the $P(s)$'s for all τ_s except $\tau_s = 0.2$ are also close to Gaussian, although a small scatter exists in the PDF width. The PDF $P(s)$ for $\tau_s = 0.2$ is the narrowest; however, the reason for this is unknown. In Fig. 6(b), for the low-pass-filtered case, all the PDFs except $\tau_s = \infty$ nearly collapse and decay faster than a Gaussian distribution. This can be explained as follows. For the velocity, most of the excitation of u_3 resides in the range $k < 9$, which results in a relatively large σ_u, leading to a cutoff at the tail of $P(u_3)$. Consider the time evolution of s along the trajectory of a fluid blob convected with velocity u_3. The time coherence of s excitation by $\Gamma_s u_3$ is limited to timescales on the order of τ_s, because $\tau_s < \tau_f(k)$. Therefore, the amplitudes of s fluctuations are $\Gamma_s u_3 \tau_s \propto u_3$, such that the PDF width decreases. In contrast, when $\tau_s = \infty$, s in the fluid blob can experience long-time coherence

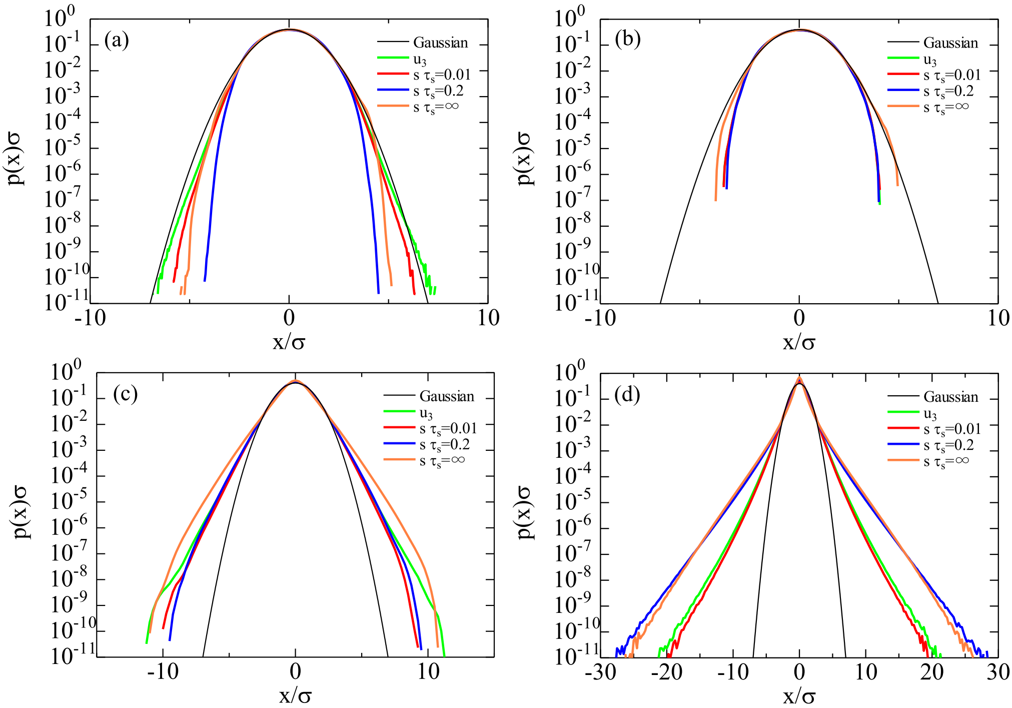

FIG. 6. Normalized PDFs for the filtered fields from LES Run L3. PDFs for (a) total, (b) low-pass-filtered ($k < 9$), (c) band-pass-filtered ($9 < k < 24$), and (d) high-pass-filtered ($k > 24$) velocity and scalar fields for $\tau_s = 0.01$, 0.2, and ∞. The black thin line indicates the Gaussian distribution.

of u_3. In other words, the fluctuations in s can accumulate over time, leading to a wider PDF. For the filtered band $9 < k < 24$ in Fig. 6(c), all PDF tails are longer than those of the Gaussian, but the trend of $P(s)$ being close to $P(u_3)$ is similar to that shown in Fig. 6(b). In the high-pass-filtered case, as shown in Fig. 6(d), all PDF tails are significantly longer than the Gaussian tails, indicating that the supersaturation field at small scales is intermittent. The closeness of $P(s)$ for $\tau_s = 0.01$ to $P(u_3)$ is due to the fact that s is determined mostly by u_3. The tails of $P(s)$ for $\tau_s = 0.2$ and ∞ are significantly wider than those for the other cases. This is because for $k > 24$, the characteristic time of s is given by $\tau_f(k)$, which is shorter than $\tau_s = 0.2$, as shown in Fig. 4(c). Thus, s behaves in the same way as in the case of $\tau_s = \infty$, whereas the scalar at small scales is more intermittent than the velocity.

The longer tail of $P(s)$ at small scales indicates strong fluctuations such that the ambient supersaturation experienced by the cloud droplets varies significantly. Therefore, the resulting distribution of the droplet radius during the initial phase of growth becomes wider. This suggests that in Langevin modeling of droplet evolution, the Gaussianity of the random noise for supersaturation is questionable, and the intermittent effects of supersaturation at small scales should be considered.

VII. SUMMARY

We investigated the variance spectrum $E_s(k)$ for supersaturation as a function of the phase-relaxation time τ_s in cloud turbulence using DNS and spectral LES, with an emphasis on whether the two $-5/3$ power-law spectra coexist at high Reynolds numbers. The DNS results indicated that as τ_s decreased, $E_s(k)$ tended to align with $E(k) \propto k^{-5/3}$ at low wave numbers; however, $E_s(k) \propto k^{-5/3}$ at high wave numbers was not observed because of dissipation by molecular viscosity, and diffusivity. To extend the inertial-convective range over the entire wave-number range used in the simulations,

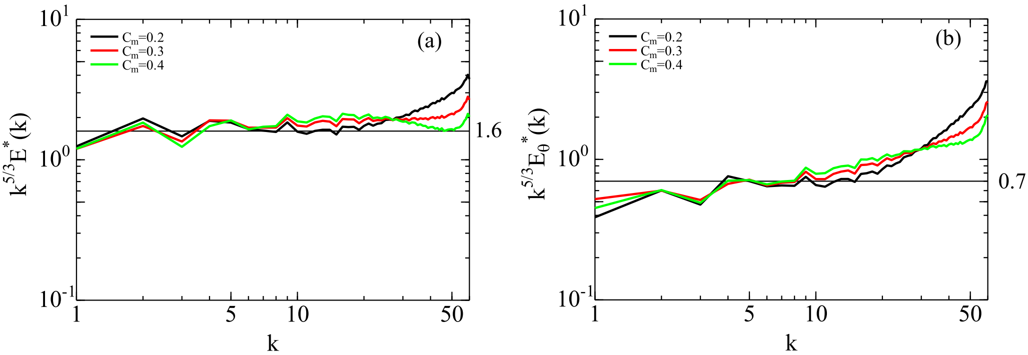

FIG. 7. Compensated spectra of (a) kinetic energy and (b) scalar variance for $C_m = 0.2, 0.3\ 0.4$, and $\tau_s = \infty$ with 128^3 grid points in LES using type 1 eddy diffusivity.

we developed a spectral eddy diffusivity model. For a passive scalar (supersaturation) with no relaxation time, the conventional eddy diffusivity could not reproduce the $k^{-5/3}$ spectrum over the entire wave-number range as shown in Fig. 7(b), and a correction was introduced to generate the $k^{-5/3}$ spectrum. We performed a set of LESs of supersaturation with modified eddy diffusivity by varying τ_s. We found that at a low $k < k_s$, the variance spectrum $E_s(k)$ tended to align with $(2/3)E(k)$, and at $k > k_s$, $E_s(k)$ followed the Obukhov-Corrsin spectrum, as theoretically predicted. The transition between the two $E_s(k)$'s occurred over approximately one decade of wave numbers. The PDFs of u_3 and s were also studied. The PDF of the low-pass-filtered supersaturation followed a sub-Gaussian distribution, whereas that of the high-pass-filtered supersaturation exhibited long tails, indicating intermittency. Modeling the evolution of cloud droplets by considering two $k^{-5/3}$ spectra and non-Gaussian supersaturation statistics is a significant challenge for future cloud turbulence studies.

The importance of resolving the two $k^{-5/3}$ ranges is that it allows cloud models to account for the scale-dependent nature of supersaturation. We found that the extent of these ranges changes depending on the relaxation time, and that the fluctuations in the high-wave-number range are intermittent with broader PDF tails. In cloud-scale simulations, understanding which range is being resolved is essential for a more accurate computation of the droplet size distribution, which is key to a better prediction of rain initiation. Furthermore, incorporating our specific eddy diffusivity model into the cloud turbulence modeling, and integrating the fine-scale intermittency of the supersaturation into microphysical models, are vital for improving the accuracy of cloud lifecycles and precipitation predictions.

ACKNOWLEDGMENTS

The authors acknowledge support from Japan Society for the Promotion of Science (JSPS) KAKENHI (Grants No. JP20H00225, No. JP23K22674, and No. JP25K01161). The authors used Fugaku computational resources provided by RIKEN through the HPCI System Research Project (hp240059, hp250029, and hp250129). They also acknowledge support from Large-scale Data Analyzing and Information Systems (JHPCN, jh240020) and National Institute for Fusion Science, Japan (NIFS23KISS033).

DATA AVAILABILITY

The data that support the findings of this article are not publicly available upon publication because it is not technically feasible and/or the cost of preparing, depositing, and hosting the data would be prohibitive within the terms of this research project. The data are available from the authors upon reasonable request.

APPENDIX A: PHASE-RELAXATION TIME

We briefly describe the derivation of Eq. (1) and the phase-relaxation time. For details, please refer to [7]. The equation for the water-vapor mixing ratio $q_\mathrm{v} = m_\mathrm{v}/m_\mathrm{a}$ (where m_v and m_a denote the masses of water vapor and dry air, respectively, in a small volume δV) is

$$\frac{\partial q_\mathrm{v}}{\partial t} + \boldsymbol{u}\cdot\nabla q_\mathrm{v} = \kappa_\mathrm{v}\nabla^2 q_\mathrm{v} - C_\mathrm{d} + \Gamma_q u_3, \tag{A1}$$

where κ_v denotes the molecular diffusivity of water vapor, C_d denotes the condensation rate, and Γ_q denotes the mean uniform vertical gradient of the water-vapor mixing ratio. The liquid-water mixing ratio $q_\mathrm{l} = m_\mathrm{l}/m_\mathrm{a}$, where m_l denotes the mass of liquid water, is defined as

$$q_\mathrm{l}(\boldsymbol{x},t) = \frac{m_\mathrm{l}}{m_\mathrm{a}} = \frac{4\pi}{3}\frac{\rho_\mathrm{l}}{\rho_\mathrm{a}\delta V}\sum_{j=1}^{N_{\delta V}(\boldsymbol{x},t)} R_j^3(t), \tag{A2}$$

where ρ_l and ρ_a denote the densities of water and air, respectively, $N_{\delta V}(\boldsymbol{x},t)$ denotes the number of droplets in the volume, and R_j denotes the radius of the jth droplet. Then, C_d is defined as

$$C_\mathrm{d}(\boldsymbol{x},t) \equiv \frac{1}{m_\mathrm{a}}\frac{dm_\mathrm{l}(\boldsymbol{x},t)}{dt} = 4\pi\frac{\rho_\mathrm{l}}{\rho_\mathrm{a}\delta V}\sum_{j=1}^{N_{\delta V}(\boldsymbol{x},t)} R_j(t)K_s s(\boldsymbol{X}_j(t),t), \tag{A3}$$

and the growth of $R_j(t)$ is assumed to obey

$$R_j\frac{dR_j}{dt} = K_s s(\boldsymbol{X}_j(t),t), \tag{A4}$$

where K_s is the temperature-dependent diffusion coefficient [5], and $\boldsymbol{X}_j$ denotes the position of the jth droplet. The supersaturation at position $\boldsymbol{X}_j(t)$ is given by

$$s(\boldsymbol{X}_j(t),t) = \frac{q_\mathrm{v}(\boldsymbol{X}_j(t),t)}{q_\mathrm{vs}} - 1, \tag{A5}$$

where q_vs denotes the saturation water-vapor mixing ratio at a given temperature and pressure.

As C_d is the sum of the discrete contributions from each droplet, we consider its continuum expression to study the supersaturation variance spectrum. For this purpose, we introduce a coarse-graining operation $\mathcal{P}[\ ]$ over a cube Δ^3, defined as

$$A_\vartriangle(\boldsymbol{x},t) = \mathcal{P}[A] \equiv \frac{1}{N_\vartriangle(\boldsymbol{x},t)}\sum_{j=1}^{N_\vartriangle(\boldsymbol{x},t)} A(\boldsymbol{X}_j(t)), \tag{A6}$$

where A is any quantity attributed to a droplet at $\boldsymbol{X}_j(t)$, and the subscript $_\vartriangle$ denotes a coarse-grained quantity. The cube Δ^3 must be sufficiently large to contain a number of droplets. Accordingly, we assume Δ to be at least 0.5 cm, five times the Kolmogorov length $\overline{\eta}$ of 1 mm but still far smaller than the Taylor microscale, which is approximately 50 times the Kolmogorov length. The LWC mixing ratio $q_{l\vartriangle}(\boldsymbol{x},t)$ as a continuum is given by

$$q_{l\vartriangle}(\boldsymbol{x},t) = \mathcal{P}[q_\mathrm{l}] = \frac{4\pi}{3}\frac{\rho_\mathrm{l}}{\rho_\mathrm{a}}\frac{N_\vartriangle(\boldsymbol{x},t)}{\Delta^3}\frac{1}{N_\vartriangle(\boldsymbol{x},t)}\sum_{j=1}^{N_\vartriangle(\boldsymbol{x},t)} R_j^3(t) \approx \lambda n_\vartriangle(\boldsymbol{x},t)\overline{R}^3(t), \quad \lambda = \frac{4\pi}{3}\frac{\rho_\mathrm{l}}{\rho_\mathrm{a}}, \tag{A7}$$

where $n_\vartriangle(\boldsymbol{x},t)$ denotes the number density of droplets. On the ground of the coarse graining we replaced the local average of the cubic radius R^3 with $\overline{R}^3$ in the passage from the second equality to the third one. Similarly, the continuum representation of the condensation-evaporation rate C_{d} is

$$C_{\mathrm{d}\triangle}(\boldsymbol{x},t)=\mathcal{P}[C_{\mathrm{d}}]=\frac{4\pi}{3}\frac{\rho_{\mathrm{l}}}{\rho_{\mathrm{a}}}\frac{N_{\triangle}(\boldsymbol{x},t)}{\Delta^3}\overline{R}^3\,\frac{3K_s}{\overline{R}^2}\frac{1}{N_{\triangle}(\boldsymbol{x},t)}\sum_{j=1}^{N_{\triangle}(\boldsymbol{x},t)}\left(\frac{R_j}{\overline{R}}\right)s(\boldsymbol{X}_j(t),t)$$
$$\approx\frac{1}{\tau_{\mathrm{l}}}q_{l\triangle}(\boldsymbol{x},t)s_{\triangle}(\boldsymbol{x},t), \tag{A8}$$

where $s_{\triangle}$ denotes the coarse-grained supersaturation and $\tau_{\mathrm{l}}=\overline{R}^2/(3K_s)$ [21]. In the passage, Eq. (A7) and the approximation $(R_j\,/\,\overline{R})\approx 1$ are used. By applying the coarse-graining operation to Eq. (A1) and using Eq. (A5) to transform $q_{v\triangle}$ to $s_{\triangle}$, we obtain

$$\frac{\partial s_{\triangle}}{\partial t}+\boldsymbol{u}\cdot\boldsymbol{\nabla}s_{\triangle}=\kappa_s\nabla^2 s_{\triangle}-\frac{1}{\tau_s}s_{\triangle}+\Gamma_s u_3, \tag{A9}$$

where $\Gamma_s=\Gamma_q/q_{\mathrm{vs}}$. Equation (A9) is Eq. (1) when the subscript $_{\triangle}$ is dropped. Here, the phase-relaxation time τ_s is given by

$$\frac{1}{\tau_s}=J\frac{\overline{Q}_{\mathrm{l}}}{\tau_{\mathrm{l}}}=J(4\pi K_s\overline{n}_{\mathrm{d}}\overline{R})\left(\frac{\rho_{\mathrm{l}}}{\rho_{\mathrm{a}}}\right), \tag{A10}$$

where $\overline{n}_{\mathrm{d}}$ and $\overline{Q}_{\mathrm{l}}$ denote the mean droplet number density and mean water-vapor mixing ratio, respectively. A nondimensional constant J arises from the variation in q_{vs} with temperature [9] and

$$J=\frac{P_{\mathrm{s}}}{\xi e_{\mathrm{s}}}+\frac{\xi L_{\mathrm{v}}^2}{c_{\mathrm{p}}R_{\mathrm{d}}T^2}, \tag{A11}$$

where P_{s} denotes the static pressure, e_{s} denotes the saturation pressure, L_{v} denotes the latent heat, c_{p} denotes the specific heat at a constant pressure, T denotes the temperature, $\xi=R_{\mathrm{d}}/R_{\mathrm{v}}=0.62$, and R_{d} and R_{v} are the gas constants of dry air and water vapor, respectively. The typical value of J is 265 at $T=273$ K. The timescale τ_s is determined solely by the thermodynamic conditions and is independent of scale [21].

According to the definition $s=q_{\mathrm{v}}/q_{\mathrm{vs}}-1$ in Eq. (A5), $s=0$ corresponds to the equilibrium state where the water-vapor mixing ratio q_{v} equals the saturation mixing ratio q_{vs}. Thus, $s>0$ represents supersaturation, while $s<0$ represents subsaturation (unsaturation). By definition, $\tau_s>0$. When $s>0$, the droplet radius grows according to Eq. (A4) (condensation) whereas s in the ambient air decreases. Conversely, when $s<0$, the droplet decays (evaporation) and s increases. Therefore, the role of the linear damping is to relax s toward the equilibrium state. It is useful to estimate the crossover time τ_s and length r_s in a cloud. In a cloud observation near the mountain top of Zugspitze, at a height of about 2650 m, the data of 11 August, 2009 are reported as $\overline{n}_{\mathrm{d}}=5.32\times 10^8$ [m^{-3}], $\overline{R}=5\times 10^{-6}$ [m], and $\varepsilon\approx 8.5\times 10^{-2}$ [m^2/s^3] [22]. The phase relaxation time computed using Eq. (A10), $\rho_{\mathrm{l}}=10^3$ [kg/m^3], $\rho_{\mathrm{a}}=1.2$ [kg/m^3], and $K_s=6.7\times 10^{-11}$ [m^2/s] is $\tau_s\approx 2.0$ [s] (note that K_s is considerably smaller than the diffusion constant of the water vapor $D_{\mathrm{v}}\approx 2.6\times 10^{-5}$ [m^2/s]; see Eq. (9.31) in [5]). The value $\tau_s=2.0$ [s] is shorter than 2.9 [s] of [22]. We infer that the difference arises from the definition of the modified diffusion constant D' but the details are not described in [22]. From Eq. (12) the characteristic time at scale r in the inertial-convective range is given by $\tau_f(r)=\sqrt{4/3}K^{-1/2}\varepsilon^{-1/3}(2\pi/r)^{-2/3}$. From the definition of the crossover length $\tau_s=\tau_f(r_s)$, we have $r_s\approx 6.0$ [m], which is indeed in the inertial range because of the Kolmogorov length $\eta=(\nu_{\mathrm{a}}^3/\varepsilon)^{1/4}\approx 0.4$ [mm] for $\nu_{\mathrm{a}}=1.3\times 10^{-5}$ [m^2/s] at 0 °C. Equation (A10) means that the denser the cloud droplets are, the shorter the phase relaxation time and the crossover length become.

APPENDIX B: TWO $k^{-5/3}$ POWER-LAW SPECTRA FOR SUPERSATURATION VARIANCE

The supersaturation excitation due to the uniform gradient is symbolically written as

$$s(\boldsymbol{k},t) = \Gamma_s \int_{-\infty}^{t} \exp(-(\sigma_f(k)+\sigma_s)(t-s))u_3(\boldsymbol{k},s)\,ds, \tag{B1}$$

$$\sigma_f(k) = \frac{1}{\tau_f(k)}, \quad \sigma_s = \frac{1}{\tau_s}. \tag{B2}$$

The input to the variance spectrum in a statistically steady state is given by

$$\begin{aligned}\langle s(\boldsymbol{k},t)s(-\boldsymbol{k},t)\rangle &= 2\Gamma_s^2\langle u_3(\boldsymbol{k},t)s(-\boldsymbol{k},t)\rangle \\ &= 2\Gamma_s^2 \int_{-\infty}^{t} \exp(-(\sigma_f(k)+\sigma_s)(t-s))\langle u_3(\boldsymbol{k},t)u_3(-\boldsymbol{k},s)\rangle \\ &= 2\Gamma_s^2 \int_{-\infty}^{t} \exp(-(2\sigma_f(k)+\sigma_s)(t-s))\langle u_3(\boldsymbol{k},s)u_3(-\boldsymbol{k},s)\rangle. \end{aligned} \tag{B3}$$

In the passage from the second to the third line, we assumed that the two-time correlation function of the turbulent velocity in steady state follows

$$\langle u_3(\boldsymbol{k},t)u_3(-\boldsymbol{k},s)\rangle = \exp(-\sigma_f(k)(t-s))\langle u_3(\boldsymbol{k})u_3(-\boldsymbol{k})\rangle. \tag{B4}$$

The isotropic sector of the input spectrum is obtained by summing over the spherical shell with radius k as

$$F_s(k) = \frac{4}{3}\Gamma_s^2\tau(k)E(k), \quad \frac{1}{\tau(k)} = \frac{2}{\tau_f(k)} + \frac{1}{\tau_s}, \tag{B5}$$

which is the right-hand side of Eq. (34).

Let us consider Eq. (34). For $k \ll k_s$, because $\tau_s \ll \tau_f(k)$, $2E_s(k)/\tau_s$ balances $\frac{4}{3}\Gamma_s^2\tau_s E(k)$ of the input term; thus $E_s(k) \approx (2/3)(\Gamma_s\tau_s)^2E(k)$. For $k_s \ll k$, because $\tau_s \gg \tau_f(k)$, the $\partial\Pi(k)/\partial k$ term becomes dominant in this range and balances the total input due to the kinetic energy from k_s to k. Integrating Eq. (B5) over k and noting that $\tau_f(k)E(k) \propto k^{-7/3}$ in the inertial range and that the largest contribution to the integral over k comes from the wave number near k_s, we obtain

$$\Pi_s(k) \approx \frac{2}{3}\Gamma_s^2 \int_{k_s}^{k} \tau_f(k)E(k)dk \propto \Gamma_s^2 K k_s^{-4/3}\varepsilon^{2/3} = \chi_s \tag{B6}$$

for $k \gg k_s$. Therefore, the dynamics due to the variance transfer in the inertial-convective range prevail in this range. Noting that $\Pi_s(k) \propto kE_s(k)/\tau_f(k)$, we obtain the Obukhov-Corrsin spectrum $E_s(k) = C_{\mathrm{OC}}\chi\varepsilon^{-1/3}k^{-5/3}$. The above analysis indicates that the physical mechanisms that yield $k^{-5/3}$ differ in the two ranges: the former arises from direct excitation by the turbulent velocity field, suggesting that the statistics of s in this range are similar to those of the velocity. In contrast, the latter is established by the cascade process in spectral space and reflects the inherent nature of passive scalar fluctuations.

APPENDIX C: EDDY DIFFUSIVITY MODELS FOR A PASSIVE SCALAR IN SPECTRAL LES

We consider a passive scalar $\theta = s_\infty$ with infinite τ_s (corresponding to a passive scalar without a relaxation term). The eddy viscosity and diffusivity are defined as follows:

$$T^>(k) = -2\nu_T(k|k_c)k^2E^<(k), \tag{C1}$$

$$T_\theta^>(k) = -2\kappa_T(k|k_c)k^2E_\theta^<(k), \tag{C2}$$

respectively, where $T^>(k)$ and $T_\theta^>(k)$ are given by Eqs. (22) and (23).

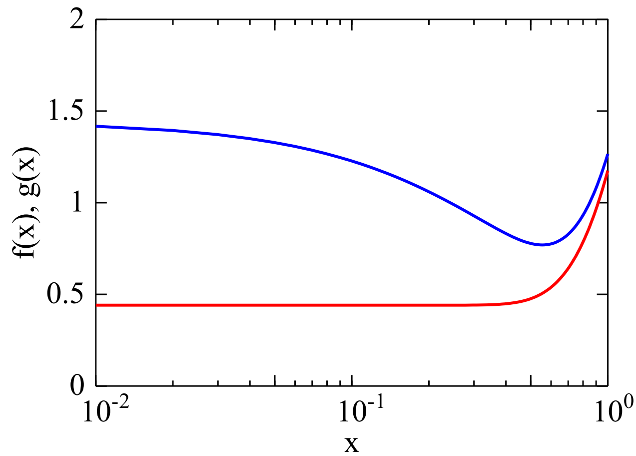

FIG. 8. Spectral eddy viscosity and diffusivity profiles. Red: $f(x)$, blue: $g(x)$.

We begin with the spectral eddy viscosity and diffusivity proposed by [20,23–27]

$$\nu_T(k|k_c) = f(k/k_c)\sqrt{E(k_c)/k_c}, \tag{C3}$$

$$\text{Type 1}: \quad \kappa_T^{(1)}(k|k_c) = \frac{1}{\mathrm{Sc}_T}\nu_T(k|k_c) = \frac{1}{\mathrm{Sc}_T}f(k/k_c)\sqrt{E(k_c)/k_c}, \tag{C4}$$

$$f(x) = C_m[0.441 + 15.2\exp(-3.03/x)], \tag{C5}$$

where C_m is an adjustable constant and the factor $\sqrt{E(k_c)/k_c}$ accounts for the velocity excitation at k_c. The eddy diffusivity is defined as the eddy viscosity divided by the turbulent Schmidt number $\mathrm{Sc}_T(k|k_c)$, which is a function of the wave number. However, in this study, we assume $\mathrm{Sc}_T = 0.72$ to be a constant. The function $f(x)$, characterized by a flat and cusplike shape, is shown in Fig. 8.

We perform the LESs by varying C_m. The objective is to determine the extent to which the $k^{-5/3}$ range of the grid-scale spectra of kinetic energy and scalar variance can be established. We introduce the following spectra:

$$E^*(k) = \varepsilon_T^{-2/3}E^<(k), \quad E_\theta^*(k) = \varepsilon_T^{1/3}\chi_T^{-1}E_\theta^<(k). \tag{C6}$$

When the $k^{-5/3}$ spectra are established at $k^{5/3}E^*(k) = K$ and $k^{5/3}E_\theta^*(k) = C_{\mathrm{OC}}$, we examine the closeness of the above spectra to the horizontal lines.

Figure 7 compares the compensated spectra computed using the eddy viscosity and diffusivity for different C_m values. The horizontal black line represents the Kolmogorov constant 1.6 for the kinetic energy spectrum in Fig. 7(a) and Obukhov-Corrsin constant 0.7 for the scalar variance spectrum in Fig. 7(b). The curves for $k^{5/3}E^*(k)$ are horizontal at a level close to K for $k < 10$, and the curve for $C_m = 0.3$ is nearly constant for almost all wave numbers, except near the cutoff wave number. For the passive scalar, the curves for $k^{5/3}E_\theta^*(k)$ are horizontal and close to C_{OC} for $k < 10$ but deviate quickly from the horizontal line for $k > 10$ compared with the kinetic energy spectrum. In Fig. 2, we infer that the slow growth of the eddy diffusivity with a decrease in wave number is the reason for the larger deviation in $k^{5/3}E_\theta^*(k)$ from the horizontal line of $C_{\mathrm{OC}} = 0.7$. Therefore, it is necessary to modify the eddy diffusivity. However, as the physical reasoning for the wave-number dependency of the eddy diffusivity at small k is not known, we explore the functional form of $f(x)$ by trial and error.

We consider two types of spectral eddy diffusivities:

$$\text{Type 2}: \quad \kappa_T^{(2)}(k|k_c) = 1.3\frac{1}{\mathrm{Sc}_T}f(k/k_c)\sqrt{E(k_c)/k_c}, \tag{C7}$$

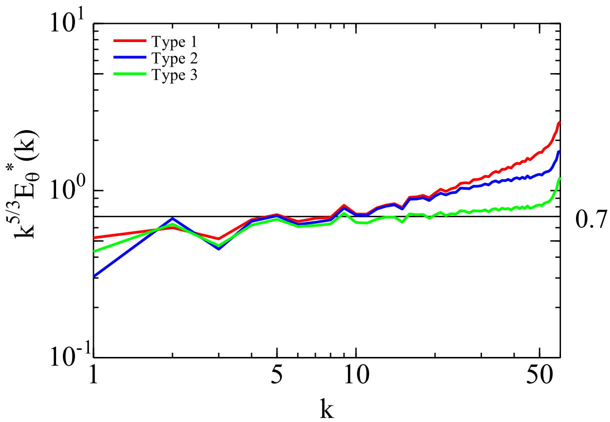

FIG. 9. Comparison of $k^{5/3}E_\theta^*(k)$ values computed using three types of eddy diffusivities.

$$\text{Type 3}: \quad \kappa_T^{(3)}(k|k_c) = 1.3\frac{1}{\mathrm{Sc}_T}g(k/k_c)\sqrt{E(k_c)/k_c}, \quad g(x) = C_m \exp(-2.4x) + f(x). \tag{C8}$$

Type 2 is augmented by a factor 1.3 compared to the eddy viscosity. The value $\mathrm{Sc}_T/1.3 \approx 0.55$ is close to the value 0.6 obtained using EDQNM [20]. Type 3 includes the term $\exp[-2.4(k/k_c)]$, which incorporates a slowly increasing trend with a decrease in wave number, as observed in the DNSs. Figure 8 shows the functions $f(x)$ and $g(x)$.

Figure 9 compares $k^{5/3}E_\theta^*(k)$ for $\tau_s = \infty$ computed using LESs with 128^3 grid points and three types of eddy diffusivities. As observed, the curve for type 3 eddy diffusivity is closest to the horizontal line for $5 < k < 50$, and the inertial-convective range for the passive scalar extends over almost all wave numbers. To study the spectrum of supersaturation variance with different finite relaxation times, we adopt the eddy viscosity given by Eq. (C3) and type 3 eddy diffusivity in Eq. (C8) with $C_m = 0.3$ for 128^3 and 512^3 grid points or $C_m = 0.6$ for 1024^3 grid points.

[1] H. Gerber, J. B. Jensen, A. B. Davis, and A. Marshak, Spectral density of cloud liquid water content at high frequencies, J. Atmos. Sci. **58**, 497 (2001).

[2] H. Siebert, K. Lehmann, and M. Wendisch, Observations of small-scale turbulence and energy dissipation rates in the cloudy boundary layer, J. Atmos. Sci. **63**, 1451 (2006).

[3] H. Siebert, R. A. Shaw, and Z. Warhaft, Small-scale velocity fluctuations and internal intermittency in marine stratocumulus clouds, J. Atmos. Sci. **67**, 262 (2010).

[4] H. Siebert, S. Gerashchenko, A. Gylfason, K. Lehmann, L. R. Collins, R. A. Shaw, and Z. Warhaft, Towards understanding the role of turbulence on droplets in clouds: *In situ* and laboratory measurements, Atmos. Res. **97**, 426 (2010).

[5] P. K. Wang, *Physics and Dynamics of Clouds and Precipitation* (Cambridge University Press, Cambridge, UK, 2013).

[6] I. Saito and T. Gotoh, Turbulence and cloud droplets in cumulus clouds, New J. Phys. **20**, 023001 (2018).

[7] T. Gotoh, I. Saito, and T. Watanabe, Spectra of supersaturation and liquid water content in cloud turbulence, Phys. Rev. Fluids **6**, 110512 (2021).

[8] A. S. Lanotte, A. Seminara, and F. Toschi, Cloud droplet growth by condensation in homogeneous isotropic turbulence, J. Atmos. Sci. **66**, 1685 (2009).

[9] G. Sardina, F. Picano, L. Brandt, and R. Caballero, Continuous growth of droplet size variance due to condensation in turbulent clouds, Phys. Rev. Lett. **115**, 184501 (2015).
[10] I. Mazin, The effect of condensation and evaporation on turbulence in clouds, Atmos. Res. **51**, 171 (1999).
[11] C. A. Jeffery, Effect of particle inertia on the viscous-convective subrange, Phys. Rev. E **61**, 6578 (2000).
[12] C. A. Jeffery, Effect of condensation and evaporation on the viscous-convective subrange, Phys. Fluids **13**, 713 (2001).
[13] C. A. Jeffery, Investigating the small scale structure of clouds using the δ correlated closure: Effect of particle inertia, condensation/evaporation and intermittency, Atmos. Res. **59-60**, 199 (2001).
[14] T. Gotoh and T. Watanabe, Statistics of transfer fluxes of the kinetic energy and scalar variance, J. Turbul. **6**, N33 (2005).
[15] T. Gotoh, D. Fukayama, and T. Nakano, Velocity field statistics in homogeneous steady turbulence obtained using a high-resolution direct numerical simulation, Phys. Fluids **14**, 1065 (2002).
[16] T. Watanabe and T. Gotoh, Statistics of a passive scalar in homogeneous turbulence, New J. Phys. **6**, 40 (2004).
[17] T. Gotoh, T. Watanabe, and Y. Suzuki, Universality and anisotropy in passive scalar fluctuations in turbulence with uniform mean gradient, J. Turbul. **12**, N48 (2011).
[18] R. H. Kraichnan, Eddy viscosity in two and three dimensions, J. Atmos. Sci. **33**, 1521 (1976).
[19] Y. Kaneda, Inertial range structure of turbulent velocity and scalar fields in a Lagrangian renormalized approximation, Phys. Fluids **29**, 701 (1986).
[20] O. Metais and M. Lesieur, Spectral large-eddy simulations of isotropic and stably-stratified turbulence, J. Fluid Mech. **239**, 157 (1992).
[21] C. Siewert, J. Bec, and G. Krstulovic, Statistical steady state in turbulent droplet condensation, J. Fluid Mech. **810**, 254 (2017).
[22] H. Siebert, R. A. Shaw, J. Ditas, T. Schmeissner, S. P. Malinowski, E. Bodenschatz, and H. Xu, High-resolution measurement of cloud microphysics and turbulence at a mountaintop station, Atmos. Meas. Tech. **8**, 3219 (2015).
[23] J. P. Chollet and M. Lesieur, Parameterization of small scales of three-dimensional isotropic turbulence utilizing spectral closures, J. Atmos. Sci. **38**, 2747 (1981).
[24] J. P. Chollet, Two-point closure used for a sub-grid scale model in large eddy simulations, in *Turbulent Shear Flows 4*, edited by L. J. S. Bradbury *et al.* (Springer, Berlin, 1985), pp. 62–72.
[25] M. Lesieur and O. Metais, New trends in large-eddy simulations of turbulence, Annu. Rev. Fluid Mech. **28**, 45 (1996).
[26] M. Lesieur, O. Metais, and P. Comte, *Large Eddy Simulations of Turbulence* (Cambridge University Press, Cambridge, 2005).
[27] J. A. Domaradzki, Large eddy simulations of high Reynolds number turbulence based on interscale energy transfer among resolved scales, Phys. Rev. Fluids **6**, 044609 (2021).